Outdoor THz fading modeling by means of Gaussian Mixture Distribution

Evangelos N. Papasotiriou (vangpapasot@unipi.gr)
University of Piraeus
Alexandros-Apostolos A. Boulogeorgos
University of Piraeus
Angeliki Alexiou
University of Piraeus

Article

Keywords:

Posted Date: July 19th, 2022

DOI: https://doi.org/10.21203/rs.3.rs-1870767/v1

Outdoor THz fading modeling by means of Gaussian Mixture Distribution

Evangelos N. Papasotiriou[1,*], Alexandros–Apostolos A. Boulogeorgos[1], and Angeliki Alexiou[1]

[1]University of Piraeus research center, department of digital systems, Piraeus, 18534, Greece
[*]corresponding author e-mail: vangpapasot@unipi.gr

ABSTRACT

Terahertz (THz) band offers a vast amount of bandwidth and is envisioned to become a key enabler for a number of next generation wireless applications. In this direction, appropriate channel models, encapsulating the large and small-scale fading phenomena, need to be developed for both indoor and outdoor communications environments. The THz large-scale fading characteristics has been extensively investigated for both indoor and outdoor scenarios. The study of indoor THz small-scale fading has recently gained the momentum, while the small-scale fading of outdoor THz wireless channels has not yet been investigated. Motivated by this, this contribution introduces Gaussian mixture (MG) distribution as a suitability small-scale fading model for outdoor THz wireless links. In more detail, multiple outdoor THz wireless measurements recorded at different transceiver separation distance are feed to an expectation-maximization (EM) fitting algorithm, which returns the parameters of the MG probability density function. The fitting accuracy of the analytical GMs is evaluated in terms of the Kolmogorov-Smirnov, Kullback-Leibler (KL) and root-mean-square-error (RMSE) tests. The results reveal that as the number of mixtures increases the resulting analytical GMs perform a better fit to the empirical distributions. In addition, the KL and RMSE metrics indicate that the increase of mixtures beyond a particular number result to no significant improvement of the fitting accuracy.

Introduction

Terahertz wireless systems have been identified as a key enabler of the next generation networks era, since it can provide the required radio resources for a number of killer-applications, including wireless backhauling, mobile ad-hoc backhauling, as well as massive connectivity of bandwidth-hungry applications, like virtual and holographic reality[1,2]. Novel wireless concepts, such as the internet of everything, connected and autonomous vehicles, and unmanned aerial vehicle , are also expected to benefit from the usage of the THz band[2]. The first step towards designing and optimizing THz wireless systems is the development of indoor and outdoor channel models that can accurately capture the particularities of the propagation medium in this band. In particular, THz wireless channel model can be seen as the joint contribution of the large and small scale fading[3]. The large scale fading can be expressed in terms of the deterministic pathloss and shadowing, while the fast channel amplitude fluctuations are described in terms of the stochastic small-scale fading[3].

The large scale fading has been extensively investigated in both outdoor and indoor environments[4–19]. In more detail, urban outdoor double directional channel measurements in the range of 141.1–148.5 GHz for distances over 100 m have been conducted[4]. These measurements by means of the many identified angles of arrival and angles of departure have verified the existence of line-of-sight (LoS) and non-line-of-sight (NLoS) THz multipath components. An outdoor measurement campaign in an urban microcell environment at 140 GHz recorded omni and directional LoS and NLoS links at a maximum distance of 117.4 m[5]. Based on the aforementioned measurements, omni and directional pathloss exponent models were implemented, where the shadowing was expressed by means of a lognormal distribution. A ray-based deterministic tool has been employed to model the large scale pathloss of an urban outdoor scenario in the range of 90–200 GHz[6]. The pathloss is modeled by the pathloss exponent model, where the shadowing due to vegetation has been modeled by means of a lognormal distribution. Based on 142 GHz multiple-input-multiple-output (MIMO) urban microcell propagation measurements, the channel spatial statistics of the number of spatial clusters and the cluster power distribution have been identified[7]. A detailed spatial statistical MIMO channel generation procedure was introduced based on the empirical channel statistics. An extensive set of wireless LoS and NLoS measurements in the range of 145–146 GHz for distances between 1–100 m has been conducted[7]. Based on the measurements, the deterministic pathloss, shadowing, delay spread, angular spread and multipath component power distribution have been modeled. A vehicle to infrastructure channel has been developed for an urban scenario by means of ray tracing for the operational frequency of 110 GHz[9]. Accordingly, the channel statistics of pathloss, time-of-arrival and direction-of-arrival were characterized. An initial review on the impact of the weather conditions to the deterministic attenuation of THz wireless links has been conducted[10]. In more detail, the channel impairments caused by the water vapor, dust particles, fog, clouds and rain

were investigated. Meanwhile, deterministic THz polynomial pathloss models for the ranges of 100–450 GHz, 200–450 GHz and 275–400 GHz were developed[11,14,15]. In these models the THz channel was assumed to consist of a single deterministic LoS coefficient, which was expressed as the sum of the free space and molecular absorption loss. Various LoS and NLoS indoor measurements were performed for wireless links operating at 28 GHz and 140 GHz[12,13]. Therein, based on the received signal strength of the multipath components of the links, the millimeter wave (mmWave) and THz channels were deterministically modeled as the dB scale sum of the exponential pathloss and lognormal shadowing. A single path theoretical THz channel model for THz wireless communications within vegatation was developed[17,19]. In this model the wireless channel consists of two coefficients, namely the deterministic pathloss and the lognormal shadowing.

The indoor THz small-scale fading channel modeling has recently gained a momentum[3,12,13,16,20–27]. Specifically, for the case of a wireless backhaul THz link, the small-scale fading was theoretically modeled by means of the α–μ distribution[20,22]. Then, the system performance was quantified under different levels of transceiver hardware impairments, antennas misalignment and fading severity. Furthermore, the suitability of the α–μ distribution to describe the small-scale fading channel amplitude of indoor THz wireless channels was experimentally validated[3,26,27]. Experimental LoS and NLoS THz wireless measurements were performed in an anechoic chamber[23]. Based on this model a stochastic indoor THz channel model was developed, where the small-scale fading attenuation factor was expressed in terms of a Rayleigh or Nakagami-m distribution under NLoS and as a Rice or Nakagami-m in LoS propagation conditions, respectively. A two dimensional stochastic geometric channel model was developed for indoor THz wireless communications[24,25]. Then, a parametric multipath Rice fading model was derived. A measurement based indoor channel model for the range of 126–156 GHz considering both LoS and NLoS conditions was developed[16]. The large-scale fading was expressed in terms of the exponential pathloss and shadowing, whereas the small-scale fading amplitude was given by a novel distribution. Meanwhile, THz wireless measurements were conducted within an anechoic chamber in the range of 240–300 GHz[21]. Then, by exploiting the measurements and various fitting accuracy metrics it was concluded that the small-scale fading amplitude of the links can be accurately modeled by means of the Gamma and Gaussian mixture models.

The aforementioned contributions underline the importance of not only the large-scale, but also the small-scale fading THz channel modeling. However, to the best of the authors knowledge, no THz small-scale fading channel model in ourdoor environments have been yet published. Motivated by this, in this work, outdoor THz measurements performed in the campus area of Aalto university Finland are exploited. In more detail, multiple LoS and NLoS links were measured at different transceiver separation distances. For each link multiple channel gain measurements were recorded, which were then used to perform fitting analysis of the empirical channel gain distribution amplitude to Gaussian Mixtures (GMs) analytical distributions. The proof of the suitability of GMs to describe the small-scale fading channel gain amplitude of outdoor THz wireless links is very useful. An appropriate GM can describe complicated fading scenarios, where multiple peaks can occur in the fading amplitude of the empirical distribution[21,28]. The GM is expressed as the sum of independent Gaussian distributions. Hence, it offers mathematical tractability, which is of great importance in analytical expressions evaluations. The measurements of each link are prepocessed to obtain the channel gain of each of the recorded multipath components. Subsequently, in order to increase the number of the different channel realizations in each link, a method based on adding random phases to the path amplitudes will be employed. Then, by making use of the resulting channel realizations of each link, the empirical probability density function (PDF) and cumulative density function (CDF) are fitted to the analytical GMs. Then, the parameters and weights of each Gaussian distribution of a GM expression are obtained by fitting it to the empirical channel gain distribution of the investigated link. This is accomplished by means of the expectation maximization (EM) algorithm[21,28–30]. The accuracy of the fit of the analytical distributions to the corresponding empirical ones is quantified in terms of the Kolmogorov-Smirnov (KS), Kullback-Leibler (KL) and Root-Mean-Square-Error (RMSE) tests[31–33]. However, the evaluation of the fitting accuracy of the analytical GMs to the empirical ones is performed only in terms of the KL and RMSE tests, because for all the GMs of all the investigated links the KS yields a good fit. As a result the KS poses as a non strict fitting criterion. According to the KL and RMSE metrics for all the links it is observed that, as the number of mixtures increases the resulting analytical GMs perform a better fit to the empirical distributions. On the other hand, as the number of mixtures decreases the resulting analytical GMs perform worse in terms of fitting even for single peak empirical distributions. Furthermore, the KL and RMSE metrics indicate that the increase of mixtures above a particular threshold does not improve drastically the fitting accuracy performance of the analytical GMs to the empirical ones.

Results

Measurement setup and sites

Figure 1 illustrates the top-view of the outdoor premises of Aalto University in Finland, where the THz measurements were conducted. In more detail, each link is defined by a unique transmitter (Tx) and receiver (Rx) pair. Both the Tx and Rx were equipped with a single antenna. During each measurement session both the Tx and Rx were in fixed positions, while only the Tx-Rx pair of interest was active, i.e., no interference was induced by neighbor links. Figures. 1(a) and 1(b) shows

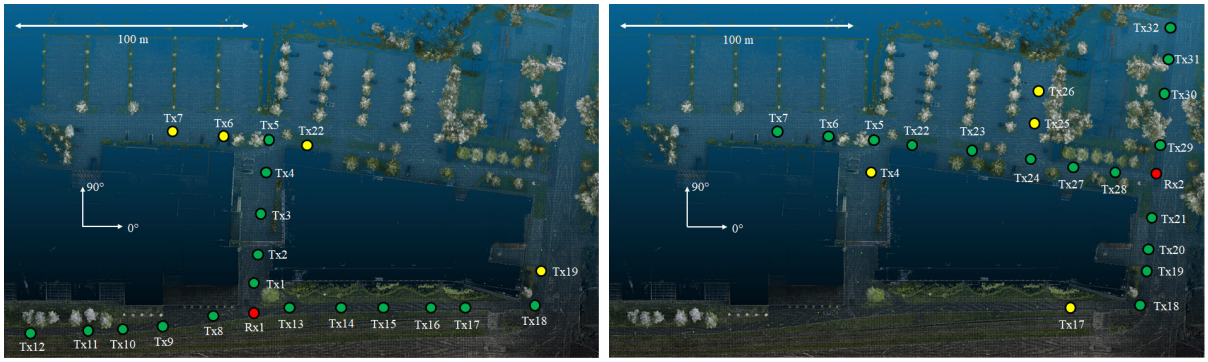

(a) Tx–Rx_1 links. **(b)** Tx–Rx_2 links.

Figure 1. Top-view of the outdoor campus premises.

that individually Rx_1 and Rx_1 were employed to perform the wireless THz measurements. The Txs marked with green dots denote a line-of-sight (LoS) link between the Tx and the Rx of interest, whereas the Txs marked with a yellow dot stand for a non-line-of-sight (NLoS) transceiver link. The THz transmissions of all the investigated links were performed at the center radio frequency (RF) of 142 GHz with a total bandwidth of 4 GHz[34]. The Tx was supplied with a transmit power of 5 dBm and the transceivers antennas heights were both equal to 1.85 m. The Rx was equipped with a sectoral horn antenna with a gain of 19 dBi, whereas the Tx was equipped with an omni-directional antenna. Also, during the measurement of each Tx–Rx link, the Rx antenna was rotated with an angular step of 5^o.

Fitting of the Gaussian mixtures to the channel gain measurements

In this section, the fading channels are approximated using the GM distribution. In more detail, Figs. 2–5 serve as an illustrative example of the fitting achieved by the analytical GMs expressions with different values of K to the empirical channel gain measurements of the investigated links. The Tables 1 and 1 quantify the fitting achieved by the GMs to the empirical measurements of the links in terms of the KL and RMSE fitting accuracy metrics. The Link, d, KL, $\widehat{\mathrm{R}}$ and K columns stand for the TX–RX link index, the transceiver antennas separation distance, the achieved KL and RMSE metric values and the corresponding K of the GM, respectively. The K GM components that yield the most accurate fit to the empirical channel gain measurements were selected by using as a criterion the minimization of the KL metric. Meanwhile, the KS metric for $K \in [1, 20]$ for all of the presented links yields a good fit. Hence it is a non strict fitting criterion and can not be employed to identify the K that corresponds to the GM with the best fit to the empirical measurements. Furthermore, the RMSE metric serves as the second best fitting criterion after the KL.

Figure 2 illustrates the statistical characterization of the TX_1–RX_1 and TX_{28}–RX_2 links. In more detail, Fig. 2(a) shows the KL values of GMs with different K for both TX_1–RX_1 and TX_{28}–RX_2. As expected, for a given link, as K increases, the KL value generally decreases. After achieving a minimum KL value, as K further increases, a short variation towards this value is observed. According to Table 1, for both of the links the maximum KL value is achieved for $K = 1$. Meanwhile, for $K = 4$ the first local minimum of KL is observed for both TX_1–RX_1 and TX_{28}–RX_2, which is equal to 0.037 and 0.123, respectively. For the TX_1–RX_1 link, the global minimum value of KL is achieved for $K = 11$, which can be found in Table 1. On the other hand, for TX_{28}–RX_2 according to Table 1 the global minimum value of KL is achieved for $K = 9$. Meanwhile, in Fig. 2(b), the RMSE metric for different values of K for both the TX_1–RX_1 and TX_{28}–RX_2 links is presented. According to Table 1, for both of the links the maximum RMSE value is achieved for $K = 1$. Meanwhile, for both the TX_1–RX_1 and TX_{28}–RX_2, $K = 4$ yields the minimum RMSE, which can be found in Table 1. The Figs 2(c) and 2(d) serve as an illustrative example of the fitting achieved by the analytical GM expressions with different K to the empirical channel gain PDFs and CDFs for the links TX_1–RX_1 and TX_{28}–RX_2, respectively. More specifically, the blue circles represent the empirical channel gain distributions of the investigated links, while the continuous and dashed lines stand for the fitted GMs of different K for the links TX_1–RX_1 and TX_{28}–RX_2, respectively. It should be noted that unless otherwise is stated the continuous and dashed lines of the same color stand for GMs with the same K. By taking into account the KL and RMSE values of Table 1 and by examining the fitting of the PDFs and CDFs of the GMs to the empirical channel gain distributions of Figs 2(c) and 2(d), it can be ascertained that the increase of K leads to analytical GM expressions that better fit the empirical ones.

Figure 3 serves as an illustrative example of the statistical characterization of the TX_4–RX_1 and TX_{16}–RX_1 links. In Fig. 3(a), the KL values of GMs with different K for both TX_4–RX_1 and TX_{16}–RX_1 are presented. It is observed that, for both TX_4–RX_1 and TX_{16}–RX_1 as K increases KL is reduced. For the interval up to $K = 7$ for both of the links KL presents a

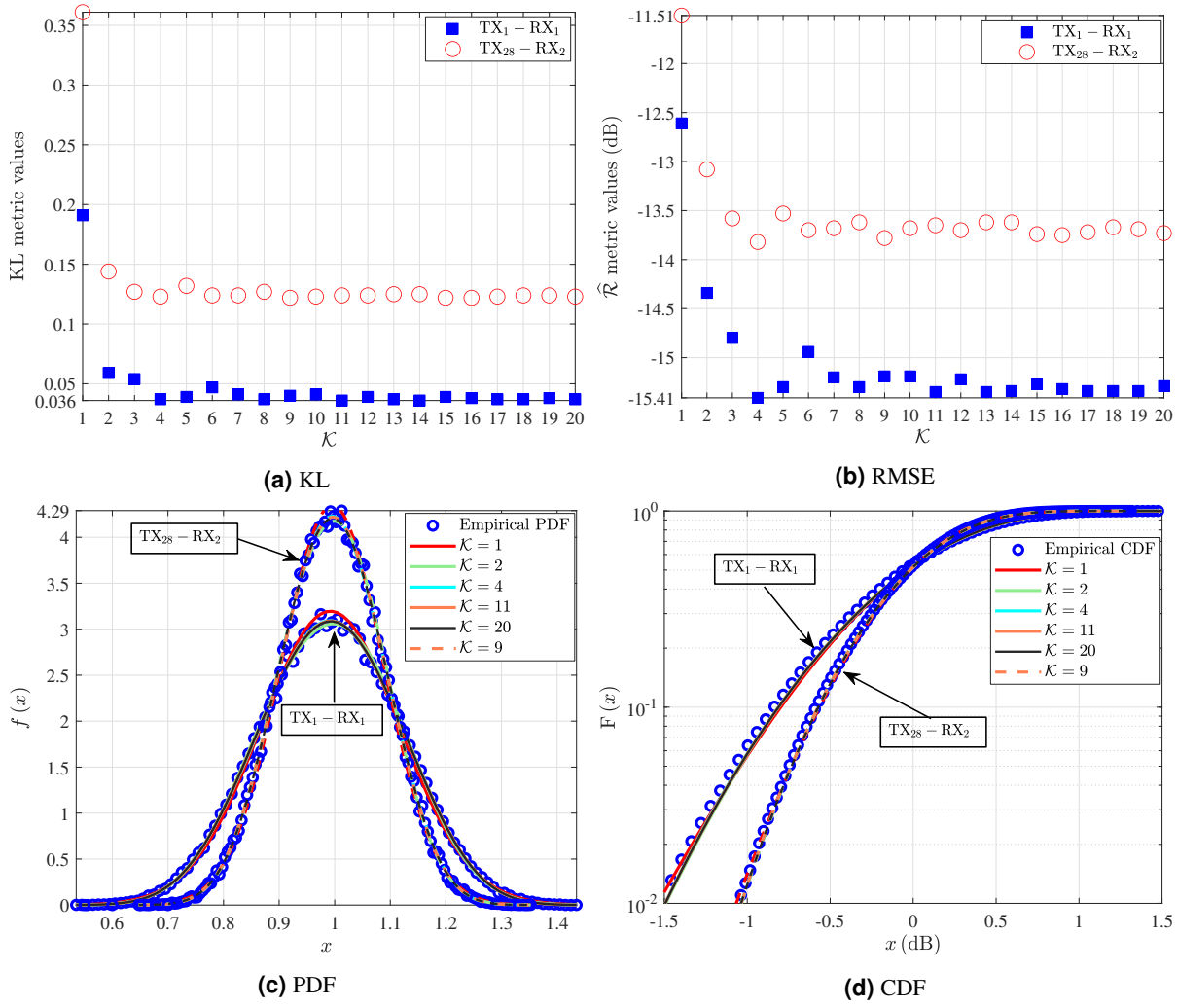

Figure 2. (a) KL and (b) $\widehat{\mathrm{R}}$ metrics for different values of K. (c) Fitting of the PDF and (d) CDF analytical expressions to the empirical channel gain data for the links TX_1–RX_1 and TX_{28}–RX_2.

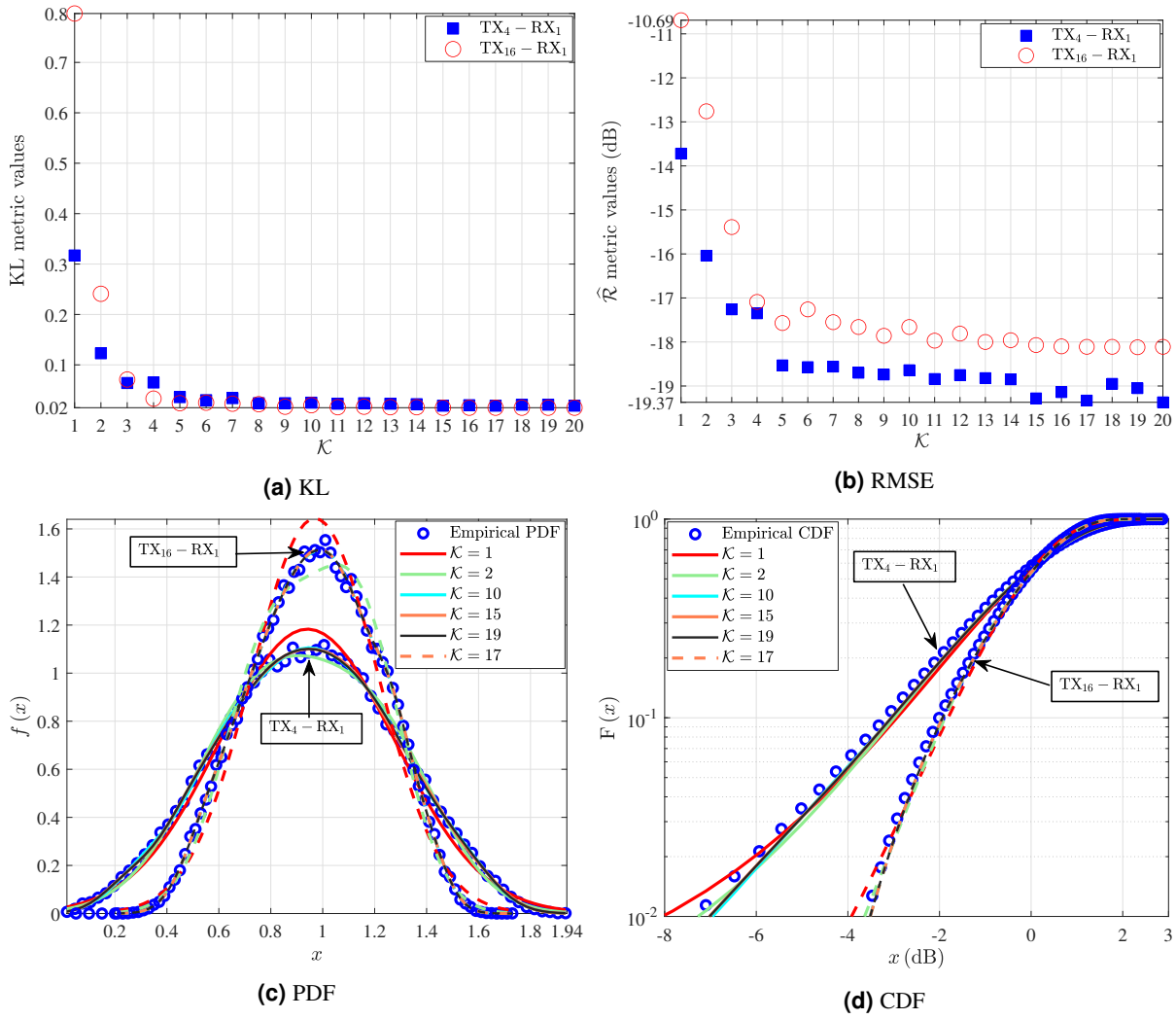

Figure 3. (a) KL and (b) $\widehat{\mathrm{R}}$ metrics for different values of K. (c) Fitting of the PDF and (d) CDF analytical expressions to the empirical channel gain data for the links TX_4–RX_1 and TX_{16}–RX_1.

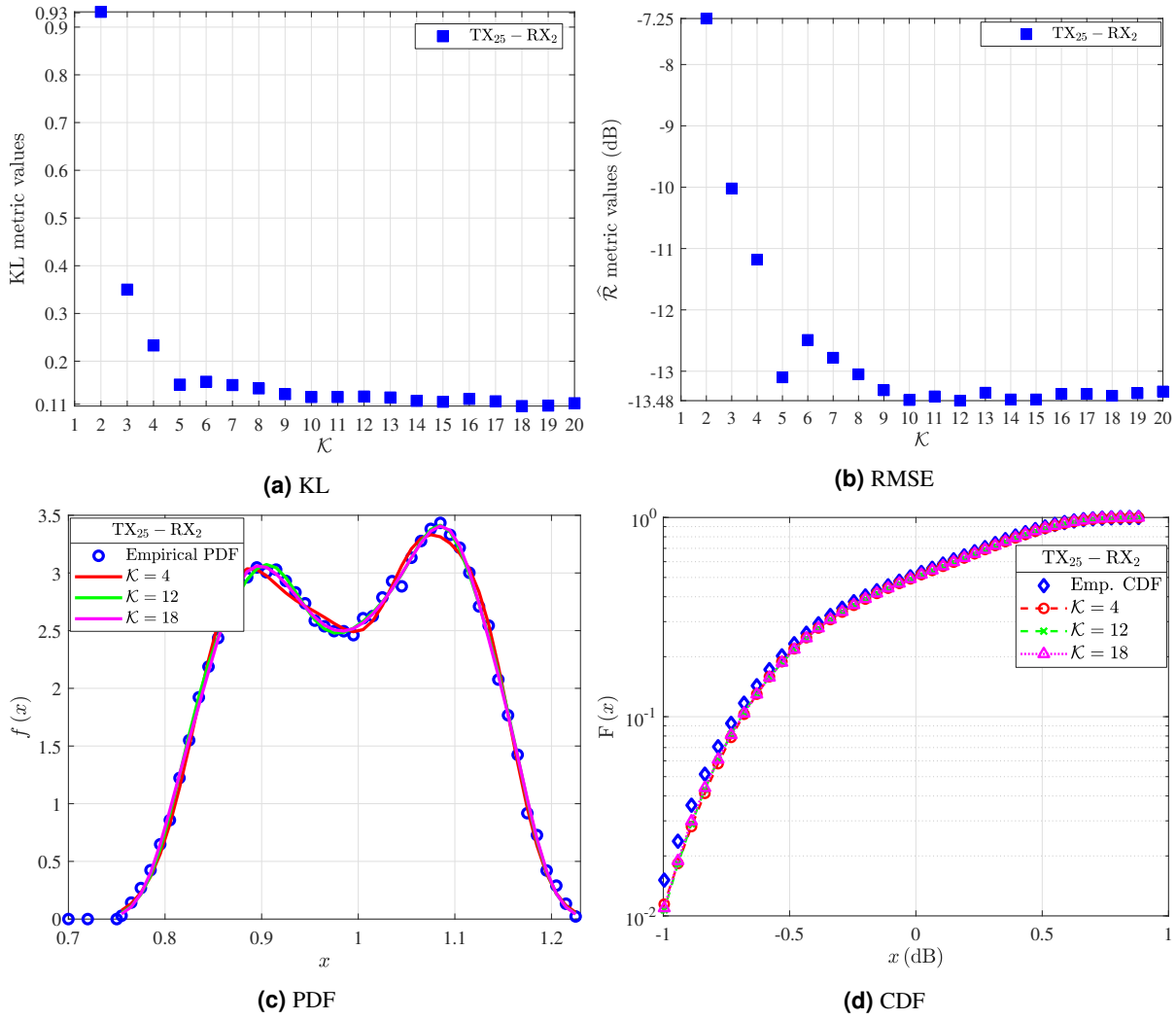

Figure 4. (a) KL and (b) $\widehat{\mathrm{R}}$ metrics for different values of K. (c) Fitting of the PDF and (d) CDF analytical expressions to the empirical channel gain data for the link TX_{25}–RX_2.

significant variation. However, when $K \in [8, 20]$ the resulting KL values stabilize. According to Table 1, the minimum KL value for both the TX_4–RX_1 and TX_{16}–RX_1 links corresponds to a GM with $K = 15$, whereas $K = 1$ leads to the worst fit. Meanwhile, Fig. 3(b) shows the RMSE metric results for different values of K for both of the links. For both TX_4–RX_1 and TX_{16}–RX_1 it is observed that as K increases the RMSE is improved. However, for both the links the RMSE values for $K \leq 10$ showcase significant variation. Table 1 suggests that, for both of the links $K = 1$ yields the worst fitting accuracy performance in terms of RMSE. Meanwhile, for TX_4–RX_1 the GMs with $K = 15$, $K = 17$, and $K = 20$ yield $\widehat{\mathrm{R}}$ equal to -19.28 (dB), -19.33 (dB), and -19.37 (dB) respectively. For TX_{16}–RX_1 the resulting RMSE values almost stabilize for $K \geq 15$. For example $K = 15$, $K = 19$, and $K = 20$ yield $\widehat{\mathrm{R}} = -18.07$ (dB), $\widehat{\mathrm{R}} = -18.12$ (dB), and $\widehat{\mathrm{R}} = -18.11$ (dB), respectively. Figs 3(c) and 3(d) present the fitting accomplished by the analytical PDFs and CDFs of GMs with different K to the empirical channel gain distributions of the links TX_4–RX_1 and TX_{16}–RX_1. The blue circles represent the empirical channel gain distributions of the investigated links, while the continuous and dashed lines stand for the fitted analytical GMs of for TX_4–RX_1 and TX_{16}–RX_1, respectively. By taking into account the KL and RMSE values of Table 1 and by observing Figs 2(c) and 2(d), it can be ascertained that the increase of K leads to analytical GM expressions that better fit the empirical ones. Moreover, it is obvious the a single Gaussian distribution (i.e. $K = 1$) can not accurately describe the empirical data.

Fig. 4 presents the statistical characterization of TX_{25}–RX_2 link. In more detail, Fig. 4(a) shows the KL achieved by GMs with different K. It is observed that as K increases the KL improves. The value of $K = 5$ yields KL $= 0.151$, which is the first local minimum. Meanwhile, for $K \geq 9$ the KL stabilizes to almost the optimum value. For example, GMs with $K = 9$, $K = 14$, $K = 18$, and $K = 20$ result KL $= 0.131$, KL $= 0.117$, KL $= 0.106$, and KL $= 0.112$ respectively. Meanwhile, according to

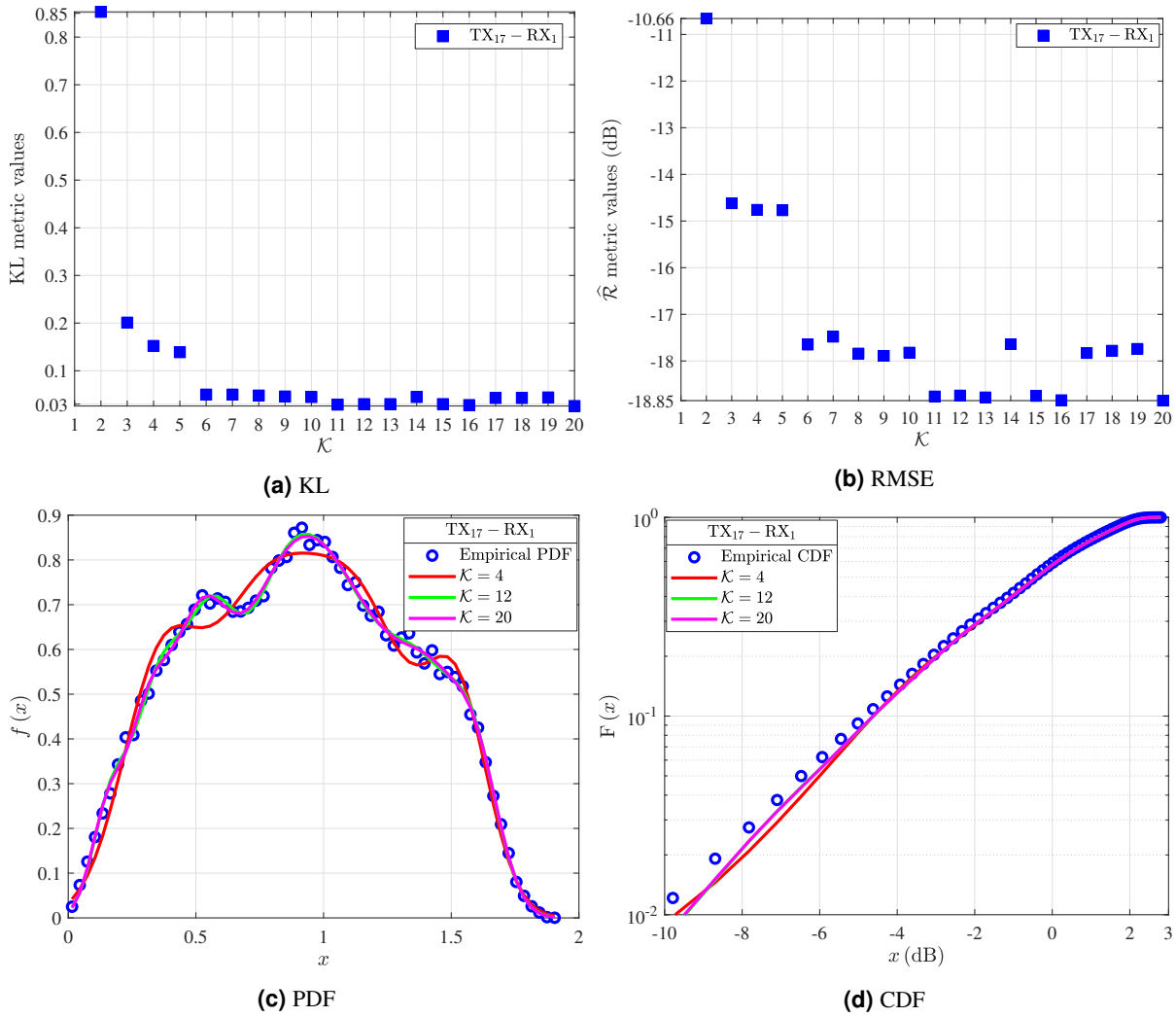

Figure 5. (a) KL and (b) $\widehat{\mathrm{R}}$ metrics for different values of K. (c) Fitting of the PDF and (d) CDF analytical expressions to the empirical channel gain data for the link TX_{17}–RX_1.

Table 1, $K = 2$ yields the maximum value of KL and hence the worst fit. In Fig. 4(b) the RMSE for GMs with different K is presented. In more detail, the first local minimum is obtained for $K = 4$ and is $\widehat{\mathrm{R}} = -11.18$ (dB), while the second local minimum results for $K = 5$ and is $\widehat{\mathrm{R}} - 13.1$ (dB). Moreover, for $K \geq 10$ the RMSE almost stabilizes to the optimum value. For example, the GMs with $K = 10$, $K = 12$, and $K = 20$ yield $\widehat{\mathrm{R}} = -13.47$ (dB), $\widehat{\mathrm{R}} = -13.48$ (dB), and $\widehat{\mathrm{R}} = -13.4$ (dB), respectively. In Figs. 4(c) and 4(d) the fitting achieved by the analytical PDF and CDF GM expressions with different values of K to the empirical channel gain distribution of TX_{25}–RX_2 are presented. In more detail, the blue circles stand for the empirical distribution of the investigated link, whereas the continuous red, green and magenta lines indicate the GM with K equal to 4, 12 and 20, respectively. The Figs. 4(c) and 4(d) illustrate that the best fit to the empirical data is accomplished by the GM with $K = 18$, which is in accordance with the KL metric results. Also, it can be conducted that, in the case an empirical PDF with multiple peaks the increase of K, leads to a GM with a higher fitting accuracy performance. In this sense, the GM with $K = 4$ performs the worst fit. As an example, for $K = 4$ the metrics are KL $= 0.233$ and $\widehat{\mathrm{R}} = -11.18$ (dB).

Fig. 5 presents the statistical characterization of TX_{17}–RX_1 link. In more detail, Fig. 5(a) shows the KL achieved by GMs with different K. It is observed that, as K increases the KL improves. In more detail, the GM with $K = 5$ yields KL $= 0.139$, which is the local minimum of the KL metric. Meanwhile, for $K \geq 11$ the KL results are almost equal. For example, for $K = 11$, $K = 15$ and $K = 20$ the resulting KL is equal to 0.029, 0.03, and 0.026, respectively. Furthermore, based on Table 1, the GM with $K = 2$ performs the worst fit in terms of the KL metric. In Fig. 5(b) the RMSE for GMs with different K is presented. It is observed that, the first and second RMSE local minima are $\widehat{\mathrm{R}} = -14.77$ (dB) and $\widehat{\mathrm{R}} = -17.89$ (dB), which are obtained for a GM with $K = 5$ and $K = 9$, respectively. The minimum RMSE according to Table 1 is accomplished for the GM with $K = 20$.

The Figs. 5(c) and 5(d) visualize the fitting achieved by the analytical PDF and CDF GMs of different K to the empirical channel gain measurements of TX_{17}–RX_1. In these Figs., the blue circles stand for the empirical distributions, whereas the continuous red, green and magenta lines indicate the analytical PDFs and CDFs of the GMs with $K = 4$, $K = 12$ and $K = 20$, respectively. The Figs. 5(c) and 5(d) demonstrate that the GMs with $K = 20$ yields the best fit. This can be verified by the KL and RMSE metric results of Table 1. Furthermore, it can be concluded that, in order to analytically describe an empirical distribution presenting multiple peaks a GM with a greater K is needed. As Fig. 5(c) demonstrates the GM with $K = 4$ performs the worst fit to the empirical data.

Discussion

The majority of the THz small-scale fading channel modeling works employ analytical distributions such as Nakagami–m, Rayleigh, Rice, α–μ and Weibull[3,23–25]. However, these distributions are capable of only describing single-peak fading channels. In this work, the suitability of modeling single and multiple peaks outdoor THz channels in terms of GMs with $K \in [1,20]$ is investigated. It is observed that for both the cases of single and multiple peaks empirical channel gain distributions the increase of K yields a GM that better fits the data. Accordingly, this is verified by the results of the KL and RMSE fitting accuracy metrics. In more detail, for all of the investigated links for the lower values of K the KL and RMSE fitting accuracy performance deteriorates. For most of the presented links the low values of K tend to yield significant variations to the KL and RMSE results. On the other hand, for all of the examined links, as K increases above a particular value the KL and RMSE fitting accuracy results tend to stabilize. This elucidates that, for any given link the best fit is accomplished by a GM with a particular value of K or higher. Hence, further increasing K will make only a slight difference on the fitting performance of the GMs to the empirical distributions.

Methods

Preprocessing of the measurement data

The RF wireless communication channel is expressed in terms of the product of one deterministic and one stochastic coefficient. The deterministic part encapsulates the large-scale effects of the propagation, i.e. the pathloss. The large-scale fading phenomena are time-invariant and remain unchanged during the wireless signal propagation. On the other hand, the stochastic channel coefficient expresses the small-scale fading characteristics of the channel, which are time and frequency dependent. The study of the small-scale fading behavior of RF wireless signals of is great importance, because it can cause unpredicted deep fades to the received signal power. As a consequence, to perform small-scale fading characterization of the channel, the effect of pathloss should be eliminated. The channel sounding performed in the outdoor campus measurements provides power angular delay profiles (PADPs) for each of the Tx–RX links. For any given link the PADPs are expressed

$$\mathrm{PADP}(\phi,t) = \sum_{i=1}^{I} GP_i \delta(\phi - \phi_i)\,\delta(t - t_i), \tag{1}$$

where ϕ_i, P_i and t_i stand for the azimuth angle at the Rx, the propagation delay gain and time of the i–th propagation path, respectively. The parameter G, known as the broadside angle, denotes the combined gains of the Tx and Rx antennas, while $\delta(\cdot)$ and I are the Dirac delta function and the total number of multipath components of a link, respectively. Subsequently, in order to eliminate the deterministic phenomenon of pathloss, the link path gain measurements by employing equation (1) to each link, are normalized to unity as

$$\zeta_i^2 = \frac{P_i}{\frac{\sum_{i=1}^{I} P_i}{I}}. \tag{2}$$

Incrementing a link channel realizations

The inherent high frequencies of the THz band lead to much higher propagation losses in comparison with the lower millimeter-wave (mmWave) and ultra-high-frequency (UHF) bands[11,13,35]. The THz free space pathloss even at distances of a few meters and a low transmission frequency can be severe. As an example for an operational frequency of 140 GHz and a wireless communication distance of one meter the free space pathloss can be in the excess of 80 dB[13,36]. Moreover, the atmospheric water vapor causes severe attenuation to the propagating THz signal[3,11]. Also, the wavelength of the emitted THz signal can be much smaller compared to the size of obstacles laid within the propagation environment[37]. As a consequence, the refraction and reflection losses of the THz band are significantly stronger when compared to lower frequency bands[35,38–40]. This leads to a significant reduction of the number of dominant rays, since the THz signal power is drastically weakened, when it is reflected or scattered two or more times[37,38]. In this sense, the ability of the THz electromagnetic wave to propagate through

Link	d (m)	KL	$\widehat{\mathrm{R}}$ (dB)	K	Link	d (m)	KL	$\widehat{\mathrm{R}}$ (dB)	K
Tx_1–Rx_1	13.72	0.191	−12.61	1	Tx_{24}–Rx_2	57.11	0.267	−10.93	1
Tx_1–Rx_1	– – – – – –	0.037	−15.41	4	Tx_{24}–Rx_2	– – – – – –	0.038	−13.99	17
Tx_1–Rx_1	– – – – – –	0.036	−15.35	11	Tx_{24}–Rx_2	– – – – – –	0.037	−13.98	18
Tx_{13}–Rx_1	16.41	0.097	−14.7	1	Tx_{15}–Rx_1	58.68	0.597	−11.44	2
Tx_{13}–Rx_1	– – – – – –	0.044	−16.64	8	Tx_{15}–Rx_1	– – – – – –	0.025	−18.17	17
Tx_{13}–Rx_1	– – – – – –	0.045	−16.71	11	Tx_{25}–Rx_2	57.71	0.932	−7.25	2
Tx_{21}–Rx_2	19.71	0.238	−11.68	1	Tx_{25}–Rx_2	– – – – – –	0.106	−13.4	18
Tx_{21}–Rx_2	– – – – – –	0.154	−12.4	4	Tx_{25}–Rx_2	– – – – – –	0.126	−13.48	12
Tx_8–Rx_1	23.1	0.109	−13.89	2	Tx_{18}–Rx_2	59.21	0.102	−13.69	1
Tx_8–Rx_1	– – – – – –	0.058	−15.38	20	Tx_{18}–Rx_2	– – – – – –	0.058	−15.15	6
Tx_2–Rx_1	27.73	0.144	−14.44	1	Tx_{18}–Rx_2	– – – – – –	0.058	−15.22	16
Tx_2–Rx_1	– – – – – –	0.026	−17.47	15	Tx_4–Rx_1	64.46	0.317	−13.72	1
Tx_2–Rx_1	– – – – – –	0.026	−17.5	19	Tx_4–Rx_1	– – – – – –	0.019	−19.28	15
Tx_{20}–Rx_2	34.1	0.152	−14.11	1	Tx_4–Rx_1	– – – – – –	0.019	−19.37	20
Tx_{20}–Rx_2	– – – – – –	0.063	−15.59	7	Tx_{32}–Rx_2	67.23	0.42	−10.51	1
Tx_{20}–Rx_2	– – – – – –	0.062	−15.59	9	Tx_{32}–Rx_2	– – – – – –	0.05	−14.12	13
Tx_{30}–Rx_2	37.25	0.219	−13	1	Tx_{32}–Rx_2	– – – – – –	0.046	−14.08	20
Tx_{30}–Rx_2	– – – – – –	0.159	−13.6	8	Tx_{11}–Rx_1	73.6	0.145	−14.29	1
Tx_{30}–Rx_2	– – – – – –	0.158	−13.57	12	Tx_{11}–Rx_1	– – – – – –	0.025	−18.42	4
Tx_{14}–Rx_1	38.15	0.061	−15.85	1	Tx_5–Rx_1	78.47	0.195	−14.97	1
Tx_{14}–Rx_1	– – – – – –	0.018	−18.03	7	Tx_5–Rx_1	– – – – – –	0.035	−17.85	14
Tx_{14}–Rx_1	– – – – – –	0.018	−18.09	10	Tx_5–Rx_1	– – – – – –	0.035	−17.88	20
Tx_{27}–Rx_2	38.6	0.263	−13.68	1	Tx_{16}–Rx_1	81.02	0.797	−10.69	1
Tx_{27}–Rx_2	– – – – – –	0.064	−15.61	17	Tx_{16}–Rx_1	– – – – – –	0.015	−18.07	15
Tx_9–Rx_1	40.02	0.331	−12.89	1	Tx_{16}–Rx_1	– – – – – –	0.015	−18.12	19
Tx_9–Rx_1	– – – – – –	0.063	−16.1	5	Tx_{23}–Rx_2	81.09	1.593	−6.74	1
Tx_9–Rx_1	– – – – – –	0.063	−16.11	11	Tx_{23}–Rx_2	– – – – – –	0.156	−10.83	20
Tx_{19}–Rx_2	42.35	0.454	−12.53	2	Tx_{17}–Rx_1	94.66	0.026	−18.85	20
Tx_{19}–Rx_2	– – – – – –	0.024	−18.61	20	Tx_{12}–Rx_1	99.61	0.283	−13.16	1
Tx_3–Rx_1	45.19	0.39	−13.69	2	Tx_{12}–Rx_1	– – – – – –	0.065	−15.38	18
Tx_3–Rx_1	– – – – – –	0.024	−18.57	18	Tx_{12}–Rx_1	– – – – – –	0.064	−15.37	20
Tx_3–Rx_1	– – – – – –	0.024	−18.62	19	Tx_{22}–Rx_2	110.1	0.528	−9.54	1
Tx_{31}–Rx_2	53.21	0.116	−13.44	1	Tx_{22}–Rx_2	– – – – – –	0.138	−12	12
Tx_{31}–Rx_2	– – – – – –	0.048	−14.78	8	Tx_{22}–Rx_2	– – – – – –	0.135	−12	19
Tx_{31}–Rx_2	– – – – – –	0.046	−14.74	9	Tx_{18}–Rx_1	127.86	0.391	−12.17	1
Tx_{10}–Rx_1	57.11	0.187	−14.35	1	Tx_{18}–Rx_1	127.86	0.064	−15.03	10
Tx_{10}–Rx_1	– – – – – –	0.015	−18.94	12	Tx_{18}–Rx_1	127.86	0.064	−15.05	20
Tx_{10}–Rx_1	– – – – – –	0.015	−18.98	13					

Table 1. Fitting accuracy metrics of GMs with different values of K.

blockages is nearly lost due to the severe propagation loss. As a result the ability of THz signals to diffract around obstacles is significantly reduced. The aforementioned remarks elucidate that, the THz band yields non-rich multipath environments, when compared for example to the mmWave band. However, still there are surfaces that can act as scatterers for propagating wireless THz signals[12,13,16,25,35]. This leads to the existence of reflected NLoS multipath components carrying a significant amount of power, which is capable of being detected by the Rx. Nevertheless, the amount of measured multipath components, utilized in our analysis, is still not adequately enough to perform small-scale fading statistics analysis for a THz wireless channel. This limitation is surpassed by generating different realizations of the transfer function. This is accomplished by changing the phases of the measured multipath components of a link[3,41]. The random phases are assumed to be stochastic are given by a uniform distribution in the interval $(0, 2\pi)$. The channel coefficient of a single-input-single-output (SISO) system can be obtained as[3,41]

$$h = \sum_{i=1} \zeta_i \exp\left(-j2\pi f t_i\right) \exp(j\psi_i), \tag{3}$$

where $\psi_i \sim U\left(0, 2\,\pi\right)$ represents the random phase of the i–th multipath component. Moreover, by assuming that the amplitude of the channel coefficients does not change dramatically among the progressing t_i, i.e. the channel can be considered as flat-fading then, $t_i = 0$[41]. Also, the term $U\left(\cdot,\cdot\right)$ is the uniform distribution operator[42].

Expectation-Maximization Based Fitting Approach

The Gaussian Mixture Model

The THz small-scale fading phenomenon has been the epicenter of many recent channel modeling studies[3,21,23,40]. Moreover, it was experimentally observed that there are wireless THz propagation scenarios, where the small-scale fading channel amplitude shows significant fluctuations[21]. In this sense, the commonly used analytical distributions that are only capable of fitting single peak distributions are now inadequate to describe the small-scale fading amplitude of such THz channels. However, by considering small-scale fading THz and lower frequency studies, mixture distributions such as Gaussian and Gamma can be employed instead[21,28,29,43].

The Gaussian mixture (GMs) have been extensively employed to describe the small-scale fading channel amplitude of RF wireless channels[21,28,29]. The PDF of the GM is expressed as

$$f_{gm}\left(x\right) = \sum_{i=1}^{K} w_i \frac{\exp\left(-\frac{(x-\mu_i)^2}{2\sigma_i^2}\right)}{\sqrt{2\pi}\sigma_i}, \tag{4}$$

where K and w_i denote the number of GM components and the weight of the i–th mixture component, respectively. The parameters μ_i and σ_i stand for the mean and standard deviation of the i–th GM component, respectively. Also, $w_i \in [0,1]$ and $\sum_{i=1}^{K} w_i = 1$. The CDF of the GM is expressed as

$$F_{gm}\left(x\right) = \frac{1}{2}\sum_{i=1}^{K} w_i \,\mathrm{Erfc}\left(\frac{\mu_i - x}{\sqrt{2}\sigma_i}\right), \tag{5}$$

where $\mathrm{Erfc}\left(\cdot\right)$ is the complementary error function[31].

The Expectation Maximization Algorithm

The weights and the parameters of the Gaussian distributions that compose the GM with the best possible fit to the empirical data must be identified by employing an appropriate method. The expectation maximization (EM) algorithm is such a method. The EM is a machine learning technique that simplifies maximum-likelihood-estimate (MLE) problems and is vastly used in calculating the parameters of mixture models[21,28].

The EM is a two step algorithm. It consists of the expectation (E) and the maximization (M) steps[30]. To operate the EM algorithm, the K number of mixtures and the vector $\mathbf{y} = (y_1, ..., y_n)$ of the n channel gain measurements of a link are required as inputs. Subsequently, the mixtures parameters are updated at the M–step during the $m+1$ iteration of the EM algorithm until the convergence criterion is met. The converge criterion is defined as

$$\left|\mathrm{L}^{[m+1]} - \mathrm{L}^{[m]}\right| > \varepsilon, \tag{6}$$

where ε stands for the desired convergence value. The term $\mathrm{L}^{[m]}$ is defined as in Eq. (7) and signifies the MLE log–likelihood at the m–th iteration of the EM algorithm

$$\mathrm{L}^{[m]} = \frac{1}{n}\sum_{i=1}^{n} \ln\left(\sum_{j=1}^{K} w_j^{[m]} \phi\left(y_i \middle| \mu_j^{[m]}, \sigma_j^{[m]}\right)\right), \tag{7}$$

where $j \in [1,K]$, $i \in [1,n]$ and $\ln(\cdot)$ stands for the natural logarithm. The term $\phi\left(y_i \middle| \mu_j^{[m]}, \sigma_j^{[m]}\right)$ is the Gaussian distribution of the j–th mixture component at the m–th iteration of the EM, which has mean and standard deviation $\mu_j^{[m]}$ and $\sigma_j^{[m]}$, respectively. Meanwhile, the E–step of the EM is implemented as

$$\gamma_{ij}^{[m]} = \frac{w_j^{[m]} \phi\left(y_i \middle| \mu_j^{[m]}, \sigma_j^{[m]}\right)}{\sum_{l=1}^{K} w_l^{[m]} \phi\left(y_i \middle| \mu_l^{[m]}, \sigma_l^{[m]}\right)}. \tag{8}$$

Uppon the completion of the E–step, the EM algorithm implements the M–step. The M–step provides the updated values of the distribution parameters of the j–th mixture at the $m+1$ step of the algorithm, which for the particular case of a GM are calculated as in Eqs. (9)–(11)

$$w_j^{[m+1]} = \frac{1}{n} \sum_{i=1}^{n} \gamma_{ij}^{[m]} \tag{9}$$

$$\mu_j^{[m+1]} = \frac{\sum_{i=1}^{n} \gamma_{ij}^{[m]} y_i}{\sum_{i=1}^{n} \gamma_{ij}^{[m]}} \tag{10}$$

$$\sigma_j^{[m+1]} = \sqrt{\frac{\sum_{i=1}^{n} \gamma_{ij}^{[m]} \left(y_i - \mu_j^{[m+1]}\right)^2}{\sum_{i=1}^{n} \gamma_{ij}^{[m]}}}. \tag{11}$$

The convergence of the EM algorithm depends on K and the initialization values of the mixtures parameters provides as input. Several methods are available to provide initialization values for the mixtures parameters. One of the most common is to employ the K-nearest-neighbour (KNN) algorithm[44].

Evaluation of the fitting

The Kolmogorov-Smirnov Test

The Kolmogorov–Smirnov goodness of fit test is defined as[31]

$$\max\left(\left|F_{emp}(x) - F_{gm}(x)\right|\right) \leq \sqrt{-\frac{1}{2N} ln\left(\frac{A}{2}\right)}, \tag{12}$$

where $F_{emp}(x)$ and N stand for the empirical values of the channel gain CDF of the examined link and the number of discrete samples of $F_{emp}(x)$, respectively. The parameter $F_{gm}(x)$ denotes the analytical CDF of the examined analytical distribution, while $A = 5\%$ is the selected significance level.

Kullback–Leibler divergence test

The Kullback–Leibler divergence test is defined as the distance between the empirical PDF $f_{emp}(x)$ and the analytical PDF $f_{gm}(x)$ of the examined distribution[32]

$$\mathrm{KL} = -\sum_{i=1}^{N} f_{emp}(x_i) \ln\left(\frac{f_{gm}(x_i)}{f_{emp}(x_i)}\right), \tag{13}$$

The closer the value of Eq. (13) to 0 the better is the fit of the analytical fading distribution to the empirical channel gain distribution.

The Root mean square error

The RMSE is defined as[33]

$$\widehat{\mathrm{R}} = \sqrt{\frac{1}{N} \sum_{i=1}^{N} \left(f_{emp}(x_i) - f_{gm}(x_i)\right)^2}. \tag{14}$$

The lower the value of $\widehat{\mathrm{R}}$ the better the fit of the analytical $f_{gm}(x)$ PDF to the empirical distribution. Also, it should be noted that the RMSE results are commonly presented in dB scale.

Data Availability

The data are owned by Aalto University Finland. Any researcher affiliated to one of the ARIADNE project partners is allowed to access and use the shared data for research purposes. The shared data must however not be made accessible to any person not affiliated with any ARIADNE project partner.

References

1. Boulogeorgos, A.-A. A., Jornet, J. M. & Alexiou, A. Directional Terahertz Communication Systems for 6G: Fact Check. *IEEE Veh. Techn. Mag.* **16**, 68–77, DOI: 10.1109/MVT.2021.3113883 (2021).
2. Alwis, C. D. *et al.* Survey on 6G Frontiers: Trends, Applications, Requirements, Technologies and Future Research. *IEEE Open J. Commun. Soc.* **2**, 836–886, DOI: 10.1109/OJCOMS.2021.3071496 (2021).
3. Papasotiriou, E. N., Boulogeorgos, A.-A. A., Haneda, K., de Guzman, M. F. & Alexiou, A. An experimentally validated fading model for THz wireless systems. *Sc. Rep.* **11**, 1–14 (2021).
4. Abbasi, N. A. *et al.* Double Directional Channel Measurements for THz Communications in an Urban Environment. In *IEEE Int. Conf. on Commun. (ICC)*, 1–6, DOI: 10.1109/ICC40277.2020.9148631 (2020).
5. Xing, Y. & Rappaport, T. S. Propagation Measurements and Path Loss Models for sub-THz in Urban Microcells. In *IEEE Int. Conf. on Commun.*, 1–6, DOI: 10.1109/ICC42927.2021.9500385 (2021).
6. Gougeon, G., Corre, Y. & Aslam, M. Z. Ray-based Deterministic Channel Modelling for sub-THz Band. In *EEE 30th Int. Symp. on Per., Ind. and Mob. Radio Commun. (PIMRC)*, 1–6, DOI: 10.1109/PIMRCW.2019.8880819 (2019).
7. Ju, S. & Rappaport, T. S. Sub-Terahertz Spatial Statistical MIMO Channel Model for Urban Microcells at 142 GHz. In *IEEE Global Commun. Conf. (GLOBECOM)*, 1–6, DOI: 10.1109/GLOBECOM46510.2021.9685929 (2021).
8. Abbasi, N. A. *et al.* Thz Band Channel Measurements and Statistical Modeling for Urban D2D Environments. *IEEE Trans. on Wir. Commun.* 1–1, DOI: 10.1109/TWC.2022.3184929 (2022).
9. Chen, Y. & Han, C. Time-Varying Channel Modeling for Low-Terahertz Urban Vehicle-to-Infrastructure Communications. In *IEEE Global Commun. Conf. (GLOBECOM)*, 1–6, DOI: 10.1109/GLOBECOM38437.2019.9013865 (2019).
10. Federici, J. F., Ma, J. & Moeller, L. Review of weather impact on outdoor terahertz wireless communication links. *Nano Commun. Net.* **10**, 13–26 (2016).
11. Kokkoniemi, J., Janne, L. & Markku, J. A line-of-sight channel model for the 100–450 gigahertz frequency band. *EURASIP J. on Wir. Commun. Net.* (2021).
12. Nguyen, S. L. H., Järveläinen, J., Karttunen, A., Haneda, K. & Putkonen, J. Comparing radio propagation channels between 28 and 140 GHz bands in a shopping mall. In *12th Eur. Conf. on Ant. and Prop. (EuCAP 2018)*, 1–5, DOI: 10.1049/cp.2018.0874 (2018).
13. Nguyen, S. L. H., Haneda, K., Järveläinen, J., Karttunen, A. & Putkonen, J. Large-Scale Parameters of Spatio-Temporal Short-Range Indoor Backhaul Channels at 140 GHz. In *2021 IEEE 93rd Veh. Techn. Conf. (VTC 2021-Spring)*, 1–6, DOI: 10.1109/VTC2021-Spring51267.2021.9448958 (2021).
14. Kokkoniemi, J., Lehtomäki, J. & Juntti, M. Simple molecular absorption loss model for 200–450 Gigahertz frequency band. In *2019 Eur. Conf. on Net. and Commun. (EuCNC)*, 219–223, DOI: 10.1109/EuCNC.2019.8801950 (2019).
15. Kokkoniemi, J., Lehtomäki, J. & Juntti, M. Simplified molecular absorption loss model for 275-400 gigahertz frequency band. In *12th Eur. Conf. on Antennas and Propagation (EuCAP)* (London, UK, 2018).
16. Pometcu, L. & D'Errico, R. An indoor channel model for high data-rate communications in D-band. *IEEE Access* **8**, 9420–9433, DOI: 10.1109/ACCESS.2019.2960614 (2020).
17. Afsharinejad, A., Davy, A., Jennings, B., Rasmann, S. & Brennan, C. A path-loss model incorporating shadowing for THz band propagation in vegetation. In *IEEE Global Communications Conference (GLOBECOM)*, 1–6, DOI: 10.1109/GLOCOM.2015.7417038 (San Diego, CA, USA, 2015).
18. Boronin, P., Petrov, V., Moltchanov, D., Koucheryavy, Y. & Jornet, J. M. Capacity and throughput analysis of nanoscale machine communication through transparency windows in the terahertz band. *Nano Commun. Networks* **5**, 72–82 (2014).
19. Afsharinejad, A., Davy, A., Jennings, B. & Brennan, C. An initial path-loss model within vegetation in the THz band. In *9th Eur. Conf. on Ant. and Prop. (EuCAP)*, 1–5 (Lisbon, Portugal, 2015).
20. Boulogeorgos, A.-A. A., Papasotiriou, E. N. & Alexiou, A. Analytical performance assessment of THz wireless systems. *IEEE Access* **7**, 11436–11453, DOI: 10.1109/ACCESS.2019.2892198 (2019).

21. Tekbıyık, K., Ekti, A. R., Kurt, G. K., Görçin, A. & Yarkan, S. Modeling and Analysis of Short Distance Sub-Terahertz Communication Channel via Mixture of Gamma Distribution. *IEEE Trans. on Veh. Techn.* **70**, 2945–2954, DOI: 10.1109/TVT.2021.3063209 (2021).

22. Boulogeorgos, A.-A. A., Papasotiriou, E. N. & Alexiou, A. Analytical performance evaluation of THz wireless fiber extenders. In *IEEE 30th An. Int. Symp. on Per., Indoor and Mob. Radio Commun. (PIMRC)*, 1–6 (Istanbul, Turkey, 2019).

23. Ekti, A. R. *et al.* Statistical modeling of propagation channels for terahertz band. In *IEEE Conf. on Standards for Commun. and Networking (CSCN)*, 275–280, DOI: 10.1109/CSCN.2017.8088634 (Helsinki, Finland, 2017).

24. Kim, S. & Zajić, A. Statistical modeling of THz scatter channels. In *9th Eur. Conf. on Antennas and Propagation (EuCAP)*, 1–5 (Lisbon, Portugal, 2015).

25. Kim, S. & Zajić, A. Statistical modeling and simulation of short-range device-to-device communication channels at sub-THz frequencies. *IEEE Trans. Wirel. Commun.* **15**, 6423–6433, DOI: 10.1109/TWC.2016.2585103 (2016).

26. Papasotiriou, E. N., Boulogeorgos, A.-A. A., Guzman, M. F. D., Haneda, K. & Alexiou, A. A New Look to THz Wireless Links: Fading Modeling and Capacity Assessment. In *Per. Ind. and Mob. Commun. (PIMRC)* (IEEE, 2021).

27. Papasotiriou, E. N., Boulogeorgos, A.-A. A. & Alexiou, A. Fading Modeling in Indoor THz Wireless Systems. In *IEEE Int. Balkan Conf. on Commun. and Netw. (BalkanCom)*, 161–165, DOI: 10.1109/BalkanCom53780.2021.9593181 (2021).

28. Selim, B., Alhussein, O., Muhaidat, S., Karagiannidis, G. K. & Liang, J. Modeling and Analysis of Wireless Channels via the Mixture of Gaussian Distribution. *IEEE Trans. on Veh. Techn.* **65**, 8309–8321, DOI: 10.1109/TVT.2015.2503351 (2016).

29. Alhussein, O. *et al.* A Generalized Mixture of Gaussians for Fading Channels. In *2015 IEEE 81st Veh. Techn. Conf. (VTC Spring)*, 1–6, DOI: 10.1109/VTCSpring.2015.7145607 (2015).

30. Dempster, A. P., Laird, N. M. & Rubin, D. B. Maximum likelihood from incomplete data via the EM algorithm. *J. Royal Stat. Soc.: Ser. B (Meth.)* **39**, 1–22 (1977).

31. Papoulis, A. & Pillai, S. *Probability, Random Variables, and Stochastic Processes*. McGraw-Hill series in electrical engineering: Commun. and signal processing (Tata McGraw-Hill, 2002).

32. MacKay, D. J. C. *Information Theory, Inference, and Learning Algorithms* (Cambridge University Press, 2003).

33. Bickel, P. J. & Doksum, K. A. *Mathematical statistics: basic ideas and selected topics, volumes I-II package*, vol. I-II (Chapman and Hall/CRC, New York, 2015), first edn.

34. de Guzman, M. F., Koivumäki, P. & Haneda, K. Double-directional multipath data at 140 GHz derived from measurement-based ray-launcher. In *2022 95th Veh. Tech. Conf. (VTC2022-Spring)*, 1–6 (Helsinki, Finland, 2022).

35. Wu, Y., Kokkoniemi, J., Han, C. & Juntti, M. Interference and Coverage Analysis for Terahertz Networks With Indoor Blockage Effects and Line-of-Sight Access Point Association. *IEEE Trans. on Wir. Commun.* **20**, 1472–1486, DOI: 10.1109/TWC.2020.3033825 (2021).

36. Jornet, J. M. & Akyildiz, I. F. Channel modeling and capacity analysis for electromagnetic wireless nanonetworks in the terahertz band. *IEEE Trans. Wir. Commun.* **10**, 3211–3221 (2011).

37. Stratidakis, G., Papasotiriou, E. N., Konstantinis, H., Boulogeorgos, A.-A. A. & Alexiou, A. Relay-based blockage and antenna misalignment mitigation in THz wireless communications. In *2nd 6G Wir. Sum. (6G SUMMIT)*, 1–4 (2020).

38. Han, C., Bicen, A. O. & Akyildiz, I. F. Multi–Ray Channel Modeling and Wideband Characterization for Wireless Communications in the Terahertz Band. *IEEE Trans. on Wir. Commun.* **14**, 2402–2412, DOI: 10.1109/TWC.2014.2386335 (2015).

39. Kokkoniemi, J., Lehtomäki, J. & Juntti, M. Stochastic Geometry Analysis for Mean Interference Power and Outage Probability in THz Networks. *IEEE Trans. on Wir. Commun.* **16**, 3017–3028, DOI: 10.1109/TWC.2017.2673844 (2017).

40. Khalid, N., Abbasi, N. A. & Akan, O. B. Statistical characterization and analysis of low-THz communication channel for 5G Internet of Things. *Nano Commun. Netw.* **22**, 100258, DOI: https://doi.org/10.1016/j.nancom.2019.100258 (2019).

41. Molisch, A. F., Steinbauer, M., Toeltsch, M., Bonek, E. & Thoma, R. S. Capacity of MIMO systems based on measured wireless channels. *IEEE J. on Sel. Areas Commun.* **20**, 561–569, DOI: 10.1109/49.995515 (2002).

42. Goldsmith, A. *Wireless communications* (Cambridge university press, 2005).

43. Al-Hmood, H. A mixture gamma distribution based performance analysis of switch and stay combining scheme over alpha -kappa-mu shadowed fading channels. In *2017 An. Conf. on New Trends in Inf. Commun. Techn. Appl. (NTICT)*, 292–297, DOI: 10.1109/NTICT.2017.7976096 (2017).

44. Vegas-Sanchez-Ferrero, G. *et al.* Gamma mixture classifier for plaque detection in intravascular ultrasonic images. *IEEE Trans. on Ultras., Ferroel., Freq. Control.* **61**, 44–61, DOI: 10.1109/TUFFC.2014.6689775 (2014).

Acknowledgements

This work has received funding from the European Commission Horizon 2020 research and innovation programme ARIADNE under grant agreement No. 871464.

Author contributions statement

E. N. P. for all the measured links processed the received power measurements, extracted the empirical distributions, performed the fitting of the analytical Gaussian Mixture distributions to the empirical ones. E. N. P., A.-A. A. B. and A. A. conducted the literature review of the existing works in the field of study. A.-A. A. B. assisted in the organization of the Results section. All authors aided in the justifications of the method section and reviewed the manuscript.

Competing Interests

The authors declare no competing interests.